

# ***Naegleria*'s mitotic spindles are built from unique tubulins and highlight core spindle features**

Katrina B Velle<sup>1</sup>, Monika Trupinić<sup>2</sup>, Arian Iveć<sup>3</sup>, Andrew Swafford<sup>1</sup>, Emily Nolton<sup>1</sup>, Luke Rice<sup>4</sup>, Iva M. Tolić<sup>2</sup>, Lillian K Fritz-Laylin<sup>1\*</sup>, Patricia Wadsworth<sup>1\*</sup>

<sup>1</sup> University of Massachusetts, Department of Biology, 611 N. Pleasant St., Amherst MA 01003, USA

<sup>2</sup> Division of Molecular Biology, Ruđer Bošković Institute, Bijenička cesta 54, 10000 Zagreb, Croatia

<sup>3</sup> Department of Physics, Faculty of Science, University of Zagreb, Bijenička cesta 32, 10000 Zagreb, Croatia

<sup>4</sup> Department of Biophysics, UT Southwestern Medical Center, Dallas, TX 75390, USA

\* Co-corresponding authors with equal contributions: [lfritzlaylin@umass.edu](mailto:lfritzlaylin@umass.edu) (L.K.F.-L.), [patw@bio.umass.edu](mailto:patw@bio.umass.edu) (PW)

## **ABSTRACT**

*Naegleria gruberi* is a unicellular eukaryote whose evolutionary distance from animals and fungi has made it useful for developing hypotheses about the last common eukaryotic ancestor. *Naegleria* amoebae lack a cytoplasmic microtubule cytoskeleton and assemble microtubules only during mitosis, and thus provides a unique system to study the evolution and functional specificity of mitotic tubulins and the resulting spindle. Previous studies showed that *Naegleria* amoebae express a divergent  $\alpha$ -tubulin during mitosis and we now show that *Naegleria* amoebae express a second mitotic  $\alpha$ - and two mitotic  $\beta$ -tubulins. The mitotic tubulins are evolutionarily divergent relative to typical  $\alpha$ - and  $\beta$ - tubulins, contain residues that suggest distinct microtubule properties, and may represent drug targets for the “brain-eating amoeba” *Naegleria fowleri*. Using quantitative light microscopy, we find that *Naegleria*'s mitotic spindle is a distinctive barrel-like structure built from a ring of microtubule bundles. Similar to those of other species, *Naegleria*'s spindle is twisted and its length increases during mitosis suggesting that these aspects of mitosis are ancestral features. Because bundle numbers change during metaphase, we hypothesize that the initial bundles represent kinetochore fibers, and secondary bundles function as bridging fibers.

## 30 INTRODUCTION

31 Cells from across the eukaryotic tree use microtubules for a wide variety of functions during  
 32 both interphase and mitosis. Interphase microtubules play essential roles establishing and  
 33 maintaining cell shape, polarity, and intracellular trafficking. During cell division, a  
 34 microtubule-based mitotic spindle self-assembles and mediates chromosome segregation. In  
 35 most well-studied organisms, the spindle is composed of functionally distinct populations of  
 36 microtubules, including: (1) kinetochore fiber microtubules that bind to kinetochores to connect  
 37 each chromosome to a single spindle pole (Inoué and Salmon, 1995); (2) non-kinetochore  
 38 microtubules that extend from the poles and overlap at the midzone, linking the two halves of  
 39 the spindle (Mastrorade *et al.*, 1993; McIntosh, Molodtsov and Ataullakhanov, 2012); and (3)  
 40 astral microtubules that extend from spindle poles toward the cell cortex. During anaphase,  
 41 kinetochore microtubules shorten, while midzone microtubules elongate to drive chromosome  
 42 segregation. A subset of midzone microtubules, called bridging fibers, contact kinetochore fibers  
 43 in each half spindle (Kajtez *et al.*, 2016). Bridging fibers contribute to the balance of tension and  
 44 compressive forces in the spindle (Kajtez *et al.*, 2016) and to chromosome motion in anaphase  
 45 (Vukušić *et al.*, 2017; Vukušić, Buđa and Tolić, 2019). Spindle microtubules are organized by  
 46 mitotic motor proteins that contribute to microtubule dynamic turnover, spindle pole organization,  
 47 chromosome congression during prometaphase and poleward motion in anaphase. The  
 48 influence of motor proteins in spindle structure is highlighted by the twist they introduce in  
 49 spindles of human cells (Novak *et al.*, 2018).

50 Interphase and mitotic microtubule functions are emergent properties of microtubule-associated  
 51 proteins as well as the subunit composition and post-translational modifications of the  
 52 microtubule polymers themselves. Eukaryotic cells typically express multi-functional tubulins  
 53 used for both interphase and mitotic functions (Raff, 1984). Human embryonic kidney cells, for  
 54 example, express high levels of one  $\alpha$ -tubulin and two 80% identical  $\beta$ -tubulins, which are used  
 55 for both interphase and mitotic functions (Vemu *et al.*, 2017). Similarly, budding yeast express a  
 56 single  $\beta$ -tubulin and two  $\alpha$ -tubulins, which share 88% sequence identity and are used for both  
 57 interphase and mitotic functions (Schatz *et al.*, 1986). As an extreme example, the unicellular  
 58 algae *Chlamydomonas* has a single  $\alpha$ - and a single  $\beta$ -tubulin gene that are used for all  
 59 microtubule functions (Johnson, 1998). Other eukaryotes, however, express unique tubulin  
 60 isotypes that are required for specific microtubule functions, including meiotic spindle assembly  
 61 in *Drosophila* oocytes (Matthews, Rees and Kaufman, 1993), axoneme formation in diverse  
 62 systems (Hoyle and Raff, 1990), and touch receptor neurons in worms (Savage *et al.*, 1989).  
 63 These specialized tubulins support the “multi-tubulin hypothesis” that posits that different  
 64 tubulins can specify microtubules with distinct cellular functions (Wilson and Borisy, 1997).

65 The multi-tubulin hypothesis was inspired by studies of *Naegleria gruberi*—a single-celled  
 66 eukaryote that diverged from the “yeast to human” lineage over a billion years ago (**Fig. 1A**)—  
 67 with the unusual ability to differentiate from a crawling amoeba to a swimming flagellate (**Fig.**  
 68 **1B**) (Fulton and Simpson, 1976). The amoeba-to-flagellate differentiation is a stress response  
 69 that involves the assembly of an entire microtubule cytoskeleton, including centrioles, flagella,  
 70 and a complete cortical microtubule array. This process includes transcription and translation of  
 71 flagellate-specific  $\alpha$ - and  $\beta$ - tubulins along with their associated microtubule binding proteins  
 72 (Fritz-Laylin, Assaf, *et al.*, 2010). The flagellate state is transient, and cells return to crawling  
 73 amoebae within 2-300 minutes (Fulton, 1993), after which time the flagellate microtubules are  
 74 disassembled and tubulin is degraded. This means that the *Naegleria* flagellate microtubules,  
 75 and the  $\alpha$ - and  $\beta$ - tubulins that comprise them, are specific for these non-mitotic microtubule

76 functions.

77 In contrast to most eukaryotic cells, however, *Naegleria* amoebae have *no* observable  
78 interphase microtubules as visualized by immunofluorescence (**Fig. 1B**) (Walsh, 2007, 2012), or  
79 by electron microscopy (Fulton and Dingle, 1971). Moreover, interphase amoebae lack tubulin  
80 transcripts (Lee and Walsh, 1988; Chung *et al.*, 2002). Previous studies have shown that  
81 *Naegleria* has a divergent  $\alpha$ -tubulin that is expressed specifically during mitosis (Chung *et al.*,  
82 2002) and that is incorporated into its intra-nuclear mitotic spindle (Walsh, 2007, 2012).  
83 Because *Naegleria* uses this specific tubulin only for spindle assembly (Chung *et al.*, 2002), it  
84 provides a unique opportunity to examine a microtubule system that is specialized for mitosis.  
85 The *Naegleria* spindle also presents an interesting divergent morphology; instead of the typical  
86 rod- or fusiform-structures found in many eukaryotes, the *Naegleria* spindle is barrel-shaped  
87 and lacks both conventional kinetochores and obvious microtubule organizing centers (Fulton  
88 and Dingle, 1971; Akiyoshi and Gull, 2014; D'Archivio and Wickstead, 2017; Drinnenberg and  
89 Akiyoshi, 2017; van Hooff *et al.*, 2017).

90 Here we test whether—in the absence of the evolutionary constraints imposed by interphase  
91 microtubule functions—*Naegleria*'s mitotic microtubule system has diverged from canonical  
92 microtubule systems. We show that, in addition to the previously reported mitotic  $\alpha$ -tubulin,  
93 *Naegleria* expresses a second mitotic  $\alpha$ -tubulin along with two mitotic  $\beta$ -tubulins. In contrast to  
94 the *Naegleria* tubulins expressed during the flagellate stage that closely resemble tubulins from  
95 heavily-studied species, the protein sequences of the *Naegleria* mitotic tubulins have diverged  
96 significantly and have unique biochemical properties. We use quantitative microscopy to show  
97 that mitotic tubulins are used to build an unusual spindle composed of a ring of regularly-spaced  
98 microtubule bundles. As mitosis proceeds, additional microtubule bundles form in the equatorial  
99 region of the spindle and—as in other eukaryotes—the spindle elongates to facilitate  
100 chromosome segregation. The organization and dynamics of the *Naegleria* spindle highlight  
101 both core aspects of mitosis and as well variable features of cell division.

## 102 RESULTS

### 103 *Naegleria* expresses divergent $\alpha$ - and $\beta$ -tubulins during mitosis

104 To determine the number and diversity of tubulins available to *Naegleria* amoebae and  
105 flagellates, we first searched for  $\alpha$ - and  $\beta$ -tubulins in the *Naegleria gruberi* genome (Fritz-Laylin,  
106 Prochnik, *et al.*, 2010). As has been previously reported, we identified 13  $\alpha$ -tubulin and 9  
107  $\beta$ -tubulin genes, some of which appeared highly divergent, while others are closely related to  
108 those of other eukaryotes (Fritz-Laylin, Prochnik, *et al.*, 2010). To further explore the diversity of  
109 *Naegleria* tubulins, we reconstructed a maximum likelihood tree of  $\alpha$ - and  $\beta$ -tubulins using  
110  $\gamma$ -tubulins as an outgroup. Briefly, we collected and aligned 1,191 tubulins sequences from 200  
111 different species (**Table S1, Datafile S1**), reconstructed a maximum likelihood tree (**Fig. S1,**  
112 **Datafile S2**), and pruned the resulting tree to more easily visualize the sequences of interest  
113 (**Fig. 1C, Datafile S3**). The tree recovers  $\alpha$ -tubulins and  $\beta$ -tubulins as two, monophyletic clades  
114 with *Naegleria* mitotic and flagellar tubulin forming evolutionarily distinct clades within each  
115 tubulin family (**Fig. 1C**).

116 The *Naegleria*  $\alpha$ - and  $\beta$ -tubulin sub-clades most closely related to animal and fungal tubulins  
117 include those that are expressed during differentiation from the amoeba to the flagellate form  
118 (Lai *et al.*, 1979; Lee and Walsh, 1988; Fritz-Laylin and Cande, 2010). These tubulins represent

119 the majority of axonemal and cytoplasmic tubulin protein in flagellates (Kowit and Fulton, 1974a,  
120 1974b; Lai, Remillard and Fulton, 1988), and are not expressed in amoebae (Lai *et al.*, 1979;  
121 Lee and Walsh, 1988; Fritz-Laylin and Cande, 2010). Flagellate  $\alpha$ -tubulins are 79-85% identical  
122 to human  $\alpha$ -tubulin A1B (ENSP00000336799) and flagellate  $\beta$ -tubulins are 74-75% identical to  
123 human  $\beta$ -tubulin B1 (ENSP00000217133) (**Fig. S2C**).

124 The second *Naegleria* tubulin sub-clades are more divergent. The second clade of  $\alpha$ -tubulins  
125 contains two sequences from each *Naegleria gruberi* and *Naegleria fowleri*, and one from each  
126 of the related species *Acrasis kona*, and *Stachyamoeba lipophora*. The two *N. gruberi*  $\alpha$ -tubulins  
127 are only 57-58% identical to human  $\alpha$ -tubulin A1B (**Fig. S2C**). Similarly, the second clade of  
128 *Naegleria*  $\beta$ -tubulins also includes *N. fowleri* and *A. kona* sequences, with *N. gruberi* sequences  
129 that are 57-58% identical to human  $\beta$ -tubulin B1.

130 Because the ortholog of the previously-reported mitotic  $\alpha$ -tubulin (from the NB-1 strain) was  
131 among the divergent  $\alpha$ -tubulins (from strain NEG-M) (Chung *et al.*, 2002; Fritz-Laylin, Prochnik,  
132 *et al.*, 2010), we predicted that the divergent *Naegleria*  $\alpha$ - and  $\beta$ -tubulins are expressed during  
133 mitosis. Consistent with this prediction, we compared expression data of amoebae (a population  
134 that includes dividing cells) and flagellates and found the conserved tubulins expressed in  
135 flagellates and the divergent tubulins expressed in amoebae (**Fig. 1D**). We confirmed this  
136 finding by comparing expression levels of the putative-mitotic tubulins in mitotically  
137 synchronized cells to control cell populations and found at least two-fold enrichment of the  
138 divergent tubulin transcripts (**Fig. S2A-B**). Together these data indicate that *Naegleria gruberi*  
139 amoebae expresses divergent  $\alpha$ - and  $\beta$ -tubulins during cell division.

# **140 *Naegleria* mitotic tubulins have diverged in ways that suggest distinct biochemical 141 properties**

142 Visual inspection of *Naegleria* mitotic and flagellate tubulin sequences suggested that the  
143 mitotic tubulins may have altered microtubule dynamics and/or binding sites for microtubule  
144 associated proteins. To more systematically assess this possibility, we quantified the divergence  
145 of mitotic and flagellate  $\alpha$ - and  $\beta$ -tubulins as a function of amino acid position. Briefly, after  
146 building master multiple sequence alignments for  $\alpha$ - and  $\beta$ -tubulins containing mitotic and  
147 flagellate tubulin sequences from *N. gruberi*, *N. fowleri*, and *A. kona* along with reference  
148 sequences from more commonly studied organisms (see Methods), we made separate 'mitotic'  
149 and 'flagellate' subalignments for each species by only retaining the mitotic or flagellate tubulin  
150 from that species (in addition to the reference sequences). We used these subalignments to  
151 measure the difference in conservation at each position, and we summarized the results with a  
152 positional 'divergence score' (**Fig. 2A**) in which negative values correspond to greater  
153 divergence at a given amino acid position (see Methods). Mitotic  $\alpha$ -tubulins have more positions  
154 with elevated divergence compared to  $\beta$ -tubulin in all three species (compare **Fig. 2A** top and  
155 bottom), although the absolute number of divergent positions differs by organism (35 positions  
156 in  $\alpha$ -tubulin vs 23 in  $\beta$ -tubulin for *N. gruberi*; 24 vs 22 for *N. fowleri*; 32 vs 27 for *A. kona*).

157 Although the positions of elevated variability are distributed throughout the tubulin fold for both  
158  $\alpha$ - and  $\beta$ -tubulin, they appear to be enriched near microtubule polymerization interfaces and  
159 surfaces displayed on the inside of the microtubule (**Fig. 2B, Fig. S3**). To quantify this  
160 impression, we tested for enrichment at longitudinal or lateral polymerization interfaces by  
161 determining whether the fraction of divergent positions near a given interface was greater than



the fraction of divergent positions across the entire sequence (see Methods). This analysis reveals that divergent positions are more enriched at lateral lattice contacts (2-3-fold increase depending on the species) than at longitudinal lattice contacts (1.1-1.9-fold, depending on the species; **Fig. 2C**). This enrichment of divergence at lattice interfaces reinforces the idea that microtubules formed from mitotic tubulins will have altered polymerization dynamics and/or distinct structural features.

Because fluorescent docetaxel—a microtubule labeling reagent derived from the microtubule-stabilizing drug taxol—appears to bind *Naegleria* flagellate tubulin but not mitotic tubulin (**Fig. 1B**), we next examined if taxol-binding residues were conserved in either of these sequences. We focused our analysis on  $\beta$ -tubulin sequences because that is where taxol binds, and we selected taxol-binding residues based on prior analyses (Gupta *et al.*, 2003) and the structure of taxol-bound microtubules (Alushin *et al.*, 2014). Important taxol-binding amino acids are conserved in flagellate but not in mitotic  $\beta$ -tubulin sequences (**Fig. S4A**). Thus, consistent with our observation that fluorescent docetaxel only labels flagellate microtubules, flagellate tubulins appear to have an intact taxol binding site, whereas the mitotic tubulins appear to have lost the ability to bind taxol.

Finally, we noted interesting sequence differences in disordered regions of the *Naegleria* tubulins. For example, the major site of  $\alpha$ -tubulin acetylation, K40, is conserved in the flagellate tubulins, but has diverged in the mitotic tubulins (**Fig. S4B**). We also characterized the length and predicted net charges of the C-terminal tubulin tails (**Fig. S4C**). The tubulin tails of both mitotic and flagellate  $\alpha$ -tubulins have lengths and net changes similar to those observed in more commonly studied tubulins. In contrast, the mitotic  $\beta$ -tubulin tails are slightly less charged than their flagellate counterparts (**Fig. S4C**). Finally, the C-terminal EY sequence in  $\alpha$ -tubulin that is recognized by regulatory factors that contain a CAP-GLY domain is notably absent from both flagellate and mitotic tubulin sequences, suggesting differences in their regulation (**Fig. S4C**). Together, these observations reinforce the notion that microtubules assembled from mitotic  $\alpha\beta$ -tubulins are likely to have different polymerization dynamics and/or binding partners compared to microtubules assembled from flagellate  $\alpha\beta$ -tubulins.

## **The *Naegleria* spindle is a hollow barrel of microtubule bundles that elongates as mitosis proceeds**

To explore whether the sequence divergence of *Naegleria*'s mitotic tubulins translates into a divergent organization of mitotic microtubules, we fixed *Naegleria* amoebae undergoing closed mitosis. We stained mitotic microtubules with anti-tubulin antibodies and DNA with DAPI, and visualized the cells using spinning disk confocal microscopy (**Fig. 3**). Consistent with previous results (Fulton and Dingle, 1971; Chung *et al.*, 2002; Fritz-Laylin *et al.*, 2011; Walsh, 2012), we find that the *Naegleria* spindle is composed of microtubule bundles and lacks obvious microtubule organizing centers (**Fig. 3**). The microtubule bundles appear to form around a ball of DNA; we refer to this stage as prophase (**Fig. 3A**). This cage-like array of microtubule bundles reorganizes into a barrel-shaped spindle with DNA aligned in a broad, hollow band at the midplane; we refer to this stage as metaphase (**Fig. 3A**). Although in some cases the spindle has a tapered morphology (**Fig. 3A**, left metaphase cell) the majority of spindles are characterized by broad, flat poles (**Fig. 3A**, middle and right metaphase cells). We also observed spindles in which the DNA is segregated to the ends of the elongated spindle, which we classified as anaphase/telophase. Compared with other stages of mitosis, few spindles were

206 detected during the early stages of chromosome segregation, suggesting that this stage  
207 occupies a small fraction of the total duration of mitosis. In contrast, cells with elongated  
208 spindles and segregated DNA were relatively common, suggesting that the late anaphase  
209 spindle is stable for some time. By quantifying spindle length and width, we infer that spindle  
210 length increases while width decreases as mitosis progresses from prophase to  
211 anaphase/telophase (**Fig. 3B**).

212 Because mitotic cells were relatively rare in asynchronous populations, we also examined  
213 mitotically synchronized cells (Fulton and Guerrini, 1969) (**Fig. S5**), and found no qualitative or  
214 quantitative differences in spindle microtubule organization between the synchronized and  
215 asynchronous cells (**Fig. S5C**). This supports previous reports that synchronization does not  
216 alter spindle morphology in *Naegleria* amoebae (Fulton and Guerrini, 1969). We therefore used  
217 cells from both synchronized and asynchronous populations for the following analyses.

218 To determine the organization of microtubule bundles in the *Naegleria* spindle, we visualized  
219 axial and transverse slices of spindles oriented both parallel and perpendicular to the coverslip  
220 (**Fig. 3C-D**). These analyses confirmed that the microtubules in the *Naegleria* metaphase  
221 spindle are organized in a ring, similar to the staves of a barrel (**Fig. 3C-D**). Previous studies  
222 have suggested that this barrel is assembled around the nucleolus, which remains intact during  
223 mitosis (*Naegleria*'s ribosomal RNA genes are encoded on a plasmid that does not condense  
224 during prophase (Fritz-Laylin *et al.*, 2011; Walsh, 2012)). To confirm the retention of the  
225 nucleolus during mitosis, we co-stained cells with anti-nucleolar and/or anti-tubulin antibodies,  
226 as well as DAPI to visualize DNA (**Fig. 3E**). Consistent with previous work, we find that the  
227 nucleolus remains throughout mitosis, at times encompassing much of the spindle volume  
228 (Walsh, 2012). The nucleolus divides before chromosome segregation, resulting in one  
229 nucleolus at each end of the spindle with the chromosomes nestled between them in a thin disk  
230 (**Fig. 3E**).

231 Comparing the dimensions and intensity of the microtubule arrays in flagellates to those in  
232 mitotic cells suggests that the spindle is composed of bundles rather than individual  
233 microtubules (**Fig. 1B**). Supporting this idea, we observed a single anaphase cell in which a  
234 microtubule bundle appears to have splayed apart, revealing at least five fluorescent elements  
235 which may represent individual microtubules (**Fig. S5E**). To estimate the number of  
236 microtubules per bundle, we fixed *Naegleria* amoeba for thin section transmission electron  
237 microscopy. Longitudinal sections through mitotic cells reveal that bundles are composed of  
238 multiple, closely-associated individual microtubules (**Fig. 3F**). We observed three to six  
239 microtubules in a single longitudinal section consistent with previous estimates in the related *N.*  
240 *fowleri* (González-Robles *et al.*, 2009). In summary, our data show that the *Naegleria* spindle is  
241 composed of a ring of microtubule bundles that elongates during chromosome segregation.

## 242 ***Naegleria* spindles have two sets of microtubule bundles**

243 Although most spindles were oriented parallel to the coverslip surface, some spindles were  
244 oriented perpendicular to the coverslip, providing improved resolution of the microtubule  
245 bundles (**Fig. 4A**). These end-on views revealed variation in the number of microtubule bundles  
246 (**Fig. 4A-C**). Some spindles have a single ring of approximately 12 evenly-spaced bundles with  
247 0.79  $\mu\text{m}$  center-to-center spacing (range: 0.42-1.90; SD: 0.28; n: 31 measurements from 3  
248 spindles). These “primary bundles” extend the entire length of the spindle (**Fig. 4A**, left, **Fig. 4B**,

top). Other spindles, however, have additional bundles adjacent to the main ring (**Fig. 4A**, middle and right, **Fig. 4B** bottom). Importantly, the number of bundles in this second class of spindles varied along the spindle axis, with additional “secondary bundles” restricted to the spindle midplane with the primary bundles extending out to the spindle ends.

If the secondary bundles were formed from new microtubule polymerization, we would expect the mid-region of metaphase spindles to have a greater amount of tubulin than the poles. We therefore quantified tubulin and DNA fluorescence intensity along horizontally-oriented spindles at each stage of mitosis (**Fig. 4D**, **Fig. S6**). The total amount of tubulin within the spindle increases as mitosis proceeds, consistent with microtubule assembly (**Fig 4E**). Metaphase spindles show variable tubulin distributions (**Fig. 4D**), with a subset having a clear peak of intensity toward the spindle midzone with “shoulders” on either side (**Fig. 4D**, rightmost metaphase). This pattern is reminiscent of the larger number of bundles that we quantified at the centers of vertically oriented spindles (**Fig. 4B**), and is consistent with secondary bundle formation involving additional microtubule assembly. Although this subset of metaphase spindles had clear “shoulders” in their tubulin distributions, other distributions were less clear-cut (**Fig. 4D**, center metaphase panel). The variability in the tubulin distribution across metaphase spindles raises the possibility that secondary bundles may form asynchronously within a spindle, consistent with cross sections of vertically-oriented spindles that show only a few secondary bundles (**Fig. 4A**, middle cell). By quantifying the maximum number of bundles per vertically-oriented spindle (**Fig. 4C**), we found that the maximum bundle number varies from ~10 to 25, with many cells showing intermediate values. This continuous distribution is consistent with asynchronous secondary bundle assembly rather than the two distinct populations we would expect for a synchronous event.

Finally, we examined the tubulin distribution in anaphase and telophase cells to determine the fate of the secondary bundles that form during metaphase. Although the tubulin intensity in these spindles was relatively uniform across the spindle midzone, we observed distinct peaks at each end of the spindle, indicating a higher density of microtubules (**Fig. 4D**, anaphase), consistent with both primary and secondary bundles remaining associated with chromosomes throughout mitosis. Together, these data suggest that secondary microtubule bundles assemble asynchronously during metaphase by new microtubule assembly and may persist through late mitosis. Based on these and other data, we hypothesize that primary bundles serve as kinetochore fibers and secondary bundles as bridging fibers (see Discussion).

## **281 The *Naegleria* spindle twists from pole-to-pole in a right-handed fashion**

The 3D reconstructions of vertically-oriented spindles revealed that the microtubule bundles curved and appeared to twist from one end of the spindle to the other (**Fig. 4A**, **Fig. 5A**, **Movie S1**, **Movie S2**). To quantify this, we traced individual bundles of metaphase spindles (**Fig. 5A**) and measured their curvature and twist by fitting a plane to the points representing the bundle and a circle that lies in this plane to the same points. We then estimated bundle curvature as one over the radius of the fit circle, and the twist as the angle between the plane and the z-axis divided by the mean distance of these points from the z-axis (**Fig. 5B**).

The resulting data show that microtubule bundles in the *Naegleria* spindle are curved ( $0.146 \pm 0.009/\mu\text{m}$ , **Fig. 5C**) and twisted ( $0.873 \pm 0.316$  degrees/ $\mu\text{m}$ ; positive values denote

right-handed and negative values left-handed twist **Fig. 5D**), with shorter bundles having more curve and twist than longer bundles (**Fig. 5C-D**). On average, the bundles were twisted in a right-handed direction, making the spindle a chiral structure with right-handed asymmetry. This result was corroborated by visual assessment of the handedness of the spindle twist. Here, if the bundles rotate counterclockwise when moving along the spindle axis in the direction towards the observer, the twist is right-handed, and vice versa. We found a mixture of left- and right-handed twist, with the majority of spindles showing a strong right-handed twist (**Fig. 5E**). Analyzing early metaphase (defined as cells with <20 bundles) and late metaphase (defined as cells with >20 bundles) cells separately suggests that bundles increase in length and decrease in curvature during metaphase (**Fig. S7A and S7D**). Right-handed twist was dominant for vertically- and horizontally-oriented spindles, and for cells in early and late metaphase (**Fig. S7B and G**), suggesting that the handedness of spindle chirality does not depend on mitotic stage or spindle orientation during imaging. Together, these data indicate that the microtubule bundles are physically linked and under rotational forces.

Other than HeLa cells, *Naegleria* are the only cell type whose spindle twist has been measured. The microtubule bundles of *Naegleria*'s spindle are less curved than those of human HeLa cell spindles, as the radius of curvature is larger for *Naegleria*,  $6.9 \pm 0.4 \mu\text{m}$ , than for the outermost bundles in HeLa cells,  $5.1 \pm 0.3 \mu\text{m}$  (Manenica *et al.*, 2020). Moreover, the radius of curvature normalized to the spindle half-length, which is equal to 1 for bundles shaped as a semicircle, is  $1.26 \pm 0.05$  for *Naegleria* and  $0.90 \pm 0.05$  for HeLa cells (Manenica *et al.*, 2020), also indicating a smaller curvature of *Naegleria* spindles. In line with the smaller curvature, the absolute value of the average spindle twist in *Naegleria* is smaller than in HeLa cells,  $0.9 \pm 0.3$  degrees/ $\mu\text{m}$  in *Naegleria* vs. 2 degrees/ $\mu\text{m}$  in HeLa (Novak *et al.*, 2018). Yet, twist of *Naegleria* spindles is more eye-catching than in HeLa cells, due to the smaller number of microtubule bundles, which are well-defined and have a uniform shape, in contrast to the less ordered distribution and shapes of bundles in HeLa cells.

## DISCUSSION

*Naegleria* amoebae represent a remarkable system with which to study microtubule biology because they do not have interphase microtubules. *Naegleria* is not the only species without interphase microtubules; the cytoplasm of interphase *Entamoeba histolytica* amoebae also has no observable microtubules (Meza, Talamás-Rohana and Vargas, 2006). In contrast to *Entamoeba*, however, *Naegleria* can differentiate into a secondary cell type, the flagellate. Here we show that *Naegleria* express unique tubulins in mitotic amoebae that are distinct from the tubulins expressed in flagellate cells. While flagellate tubulins—used to assemble both flagellar and cytoplasmic microtubules (Fulton and Kowit, 1975; Fulton and Simpson, 1976; Fulton, 1983; Lai, Remillard and Fulton, 1988; Fritz-Laylin and Cande, 2010)—are highly similar to tubulins of other eukaryotic species, the mitotic tubulins have diverged in sequence, including at key residues likely to alter microtubule structure or dynamics. Because the sequence similarity between *Naegleria* and *Acrasis* flagellate tubulin isoforms is much higher than their mitotic tubulins (Fig. S2-C), we infer that the cytoplasmic functions of tubulins may require more stringent sequence conservation than mitotic functions.

*Naegleria* mitotic microtubules assemble into a hollow, barrel-shaped mitotic spindle comprising distinct bundles, each made of multiple microtubules. Based on these observations and additional literature discussed below, we propose the following model for *Naegleria* spindle



335 elongation and chromosome segregation (**Fig. 6**): (1) Mitosis begins with the assembly of  
 336 “primary” microtubule bundles. Each primary bundle is associated with a chromosome and  
 337 functions as a pair of kinetochore fibers; (2) During metaphase, “secondary” microtubule  
 338 bundles form near the spindle midplane that function as bridging fibers, connecting kinetochore  
 339 fibers associated with sister chromatids (Simunić and Tolić, 2016; Vukušić *et al.*, 2017); (3)  
 340 chromosome-to-pole motion occurs as primary bundles depolymerize while secondary bundles  
 341 elongate to form the spindle midzone and further separate the chromosomes. Under this model,  
 342 the higher microtubule density toward the poles during late anaphase results from fluorescence  
 343 of both kinetochore and bridging fiber microtubules. While this model is consistent with our  
 344 quantitative measurements, other scenarios are also possible. For example, secondary bundles  
 345 could associate with chromosomes, functioning like kinetochore fibers, and primary bundles  
 346 could form the midzone, or each individual bundle could be composed of bridging and  
 347 kinetochore fiber microtubules, that ultimately sort into the anaphase spindle.

348 The possibility that primary bundles function as kinetochore fibers is consistent with our  
 349 previous estimate of ~12 chromosomes in *Naegleria* (Fritz-Laylin, Prochnik, *et al.*, 2010), a  
 350 value that is similar to the average number of primary bundles we observe in early metaphase  
 351 spindles (**Fig. 4**). We also observe “kinks” in the center of some spindles suggesting that each  
 352 primary bundle may be composed of two kinetochore fibers. Although conventional, trilaminar  
 353 kinetochores have not been detected using electron microscopy (**Fig. 3F**) (Fulton and Dingle,  
 354 1971), homologs of a subset of kinetochore proteins identified in other organisms are present in  
 355 the *Naegleria* genome (Akiyoshi and Gull, 2014; van Hooff *et al.*, 2017), hinting at the presence  
 356 of yet-to-be-detected kinetochores. Whether or not *Naegleria* has conventional kinetochores,  
 357 spindle assembly and chromosome movement is well established to occur in the absence of  
 358 kinetochores (Heald *et al.*, 1996; Brunet *et al.*, 1999). For example, in both mouse and *C.*  
 359 *elegans* meiotic and human mitotic spindles, lateral interactions between microtubules and  
 360 chromosomes drive chromosome congression, although chromosome-to-pole motion does  
 361 require kinetochore-microtubule interactions (Kapoor *et al.*, 2006; Mullen, Davis-Roca and  
 362 Wignall, 2019; Danlasky *et al.*, 2020).

363 Our working model posits that both anaphase A, chromosome-to-pole motion, and anaphase B  
 364 spindle elongation, contribute to chromosome segregation in *Naegleria*. The presence of short  
 365 microtubule bundles between the chromosomes and poles in anaphase spindles is consistent  
 366 with microtubule depolymerization during anaphase A, although the location and regulation of  
 367 microtubule assembly and disassembly in these cells is not yet known. Anaphase/telophase  
 368 spindles in *Naegleria* are longer than metaphase spindles, consistent with anaphase B spindle  
 369 elongation. In meiotic spindles, anaphase B is driven, at least in part, as polymerizing midzone  
 370 microtubules interact with chromosomes (Dumont, Oegema and Desai, 2010; Danlasky *et al.*,  
 371 2020). In mammalian cells, links between elongating midzone bridging microtubules and  
 372 kinetochore fibers contribute to anaphase (Vukušić *et al.*, 2017; Vukušić, Buđa and Tolić, 2019).  
 373 Although the mechanism of spindle elongation in *Naegleria* is not yet established, the  
 374 appearance of secondary bundles in the chromosome region is reminiscent of bridging fibers in  
 375 other cell types (Simunić and Tolić, 2016). This similarity suggests that interactions between  
 376 primary and secondary microtubule bundles may contribute to chromosome segregation  
 377 (Vukušić, Buđa and Tolić, 2019).

378 These bundles differentiate the *Naegleria* spindle from those of other species that typically  
 379 contain both individual and bundled microtubules. Despite this difference, microtubule bundles



in *Naegleria* and human cells both show twist, suggesting that this may be a conserved feature of eukaryotic spindles. In contrast to the left-handed chirality previously measured in human spindles (Novak *et al.*, 2018), the majority of *Naegleria* spindles are right-handed. Because *Naegleria* is only the second species whose spindle chirality has been measured, it is difficult to know whether its chirality is unusual. Regardless, the requirement of the motor activity of kinesin Eg5 in the twisting of human spindles suggests that *Naegleria* spindle twist may also depend on the activity of microtubule motors that generate torque within the bundles (Tolić, Novak and Pavin, 2019).

*Naegleria*'s evolutionary position makes it uniquely suited for identifying features of mitotic spindles that may be deeply conserved, including their bi-polarity, elongation, and twist. *Naegleria*'s position also highlights features that may be lineage-specific due to their absence in this distant species. For example, some features of animal cell spindles are missing from *Naegleria*, including obvious microtubule organizing centers as well as astral microtubules which contribute to spindle position and to cytokinesis in other cells. Whether these differences are related to the divergence of the *Naegleria* mitotic tubulins awaits further investigation.

The unique properties of these mitotic tubulins may also have practical value. Although the model species *Naegleria gruberi* is innocuous, the related *Naegleria fowleri* is the infamous "brain-eating amoeba" that causes a devastating and usually lethal brain infection (Siddiqui *et al.*, 2016). Because the divergent residues we have identified in the *Naegleria* mitotic tubulins are conserved in both *Naegleria* species but not in human tubulins (Fig. 2, Fig. S4), these residues represent potential targets for specific therapeutics that could disrupt *Naegleria* cell division to halt *in vivo* growth.

## MATERIALS AND METHODS

**Phylogenetic tree estimation:** To establish a more inclusive comparison of *Naegleria*  $\alpha$ -, and  $\beta$ -tubulins to those of other eukaryotes, 1,191 tubulins from 200 different species were analyzed (Table S1), adding sequences from *Naegleria gruberi* (Fritz-Laylin, Prochnik, *et al.*, 2010), *Naegleria fowleri* (Herman *et al.*, 2020), and *Acrasis kona* (personal communication, Sandra Baldauf, Uppsala University) to those identified as  $\alpha$ ,  $\beta$ , and  $\gamma$  tubulins using the PhyloToL pipeline (Cerón-Romero *et al.*, 2019). Prior to alignment, sequences from the same species that were 100% identical were removed, leaving only one copy before re-merging the datasets. Sequences were aligned using the PASTA iterative alignment algorithm with the MUSCLE algorithm as the aligner and merger (Mirarab *et al.*, 2015). IQ-Tree v1.16.2 was used for model selection, which indicated LG4M+R10 as the best model for reconstruction (Kalyaanamoorthy *et al.*, 2017; Minh *et al.*, 2020). Due to the size of the tree, LG4M was used to balance the accuracy of tree solving and the constraints of modern processing power. A maximum likelihood tree was reconstructed using IQ-Tree with 10,000 ultrafast bootstraps (Hoang *et al.*, 2018). 1,000 bootstraps of the approximate likelihood ratio test (Guindon *et al.*, 2010) as well as the aBayes test (Anisimova *et al.*, 2011) were then used to further test node support. The iTOL web server was used for tree visualization (Letunic and Bork, 2019).

**Characterization of *Naegleria* mitotic tubulin sequences:** To quantify the divergence of mitotic and flagellate  $\alpha$ - and  $\beta$ -tubulins from *N. gruberi*, *N. fowleri*, and *A. kona* as a function of

amino acid position, we compared them to a common reference consisting of sequences of  $\alpha$ - or  $\beta$ -tubulin sequences from commonly studied model organisms (*Homo sapiens*, *Sus scrofa*, *Bos taurus*, *Drosophila melanogaster*, *Mus musculus*, *Saccharomyces cerevisiae*, *Schizosaccharomyces pombe*, and *Chlamydomonas reinhardtii*). Multiple sequence alignments were first prepared for  $\alpha$ - and  $\beta$ -tubulin using ClustalOmega (Madeira *et al.*, 2019). These ‘master’ alignments contained the reference sequences as well as mitotic and flagellate sequences from the three species of interest. Separate “flagellate” and “mitotic” subalignments were then prepared for each species by only retaining flagellate or mitotic sequences from a given species, in addition to the common reference sequences. We quantified sequence conservation/divergence as a function of amino acid position in these subalignments using the AL2CO server (Pei and Grishin, 2001), using normalized sum of pairs scoring (BLOSUM62 weighting) and otherwise default settings. The resulting conservation scores are normalized so that completely conserved positions return the same score regardless of the identity of the conserved amino acid; lower scores (including negative scores) correspond to less conservation. To assess differences in conservation between mitotic and flagellate sequences, the flagellate score was subtracted from the mitotic score at each amino acid position. The resulting difference score is close to zero when a position in the mitotic and flagellate sequences is equally conserved/diverged relative to the set of references sequences; it is positive when the mitotic sequence is less divergent, and negative when the mitotic sequence is more divergent. To identify the positions where the divergence of mitotic sequences was greater than flagellate sequences, the conservation score at each position was divided by the standard deviation of scores over all positions. We focused our subsequent analysis on especially divergent positions, which we defined as those where the relative divergence was greater than two standard deviations away from the mean (**Fig. 2A**).

We used PyMol (citation: The PyMOL Molecular Graphics System, Version 2.4.1 Schrödinger, LLC) and a cryo-EM structure of  $\alpha\beta$ -tubulin in a microtubule (PDB code 6O2R (Eshun-Wilson *et al.*, 2019)) to assess if the especially divergent positions in mitotic tubulins were enriched near microtubule polymerization interfaces (**Fig. 2B-C**, **Fig. S3**). To obtain the overall fraction of especially divergent positions per chain, the number of especially divergent positions in  $\alpha$ - and  $\beta$ -tubulin was divided by the total number of amino acids. To calculate the proportion of divergent positions near lateral or longitudinal interfaces, we used distance based selections to identify the amino acids within a cutoff distance of a lateral or longitudinal lattice neighbor, and calculated the ratio of divergent to total positions within this subset.

**Cell and bacterial culture:** *Naegleria amoebae* (strain NEG, ATCC strain 30223) and their food source *Aerobacter aerogenes* (a gift from the laboratory of Chandler Fulton, Brandeis University) were routinely cultured following previously established protocols (Heuser and Razavi, 1970). Briefly, *A. aerogenes* were regularly streaked from a frozen glycerol stock, and single colonies were grown stationary at room temperature in penassay broth (Difco antibiotic medium 3). Liquid cultures were used to grow lawns of *A. aerogenes* overnight on NM plates (2 g/L Difco Bacto peptone, 2 g/L glucose, 1.5 g/L K<sub>2</sub>HPO<sub>4</sub>, 1 g/L KH<sub>2</sub>PO<sub>4</sub>, 20 g/L agar). Lawns were inoculated with a loopful of NEG amoebae or cysts to create an edge plate (from a previous edge or cyst plate). Plates were sealed with parafilm, inverted, and incubated for 1-3 days at 28 °C. For starvation-induced differentiation (**Fig 1B**), cells were shocked with ice cold 2 mM Tris, and transferred to a shaking flask at 28 °C for 1 h.

**Mitotic synchronies:** To obtain a population of synchronized cells, we modified a previously

published method (Fulton and Guerrini, 1969) to cause a heat-induced mitotic arrest. Briefly, the day before the synchrony, a lawn of *A. aerogenes* was collected in 10 ml of TrisMg (2 mM Tris + 10 mM MgSO<sub>4</sub>), pelleted, resuspended in 20 ml TrisMg. 10 ml of the bacterial solution were transferred into a 125 ml flask. 2-8x10<sup>5</sup> amoebae were added to the flask and covered with foil, and the culture was incubated in a shaking water bath overnight (125 RPM, 30 °C). The morning of the synchrony, two additional lawns of *A. aerogenes* were collected, pelleted, and resuspended in 40 ml TrisMg. This solution was added to the flask with *Naegleria*, and allowed to shake for 3 minutes to thoroughly mix. This mixture was divided into 2 new (uncovered) flasks, one “control” and one “experimental,” and cell counts were taken with a hemocytometer. Cells were counted approximately every 20 min, and once the cells had doubled from their starting concentration, a sample was taken for quantitative real time PCR (qPCR) analysis (see next section), and the experimental flask was moved to a 38.5 ±0.5 °C water bath. Cells were counted from each flask, and when the control flask had doubled again, another sample was taken from each flask for qPCR, and then the experimental flask was shifted back to 30 °C. Samples were taken from the experimental flask after shifting back to 30 °C to fix and stain cells for mitotic spindles.

**Analysis of tubulin gene expression:** Samples were collected from each flask prior to the temperature shift (pre-shift, control and experimental flasks), and again after incubation at 38 °C (or 30 °C for the control flask) but before shifting back to 30 °C. For each sample, 5 ml of cells were spun down at 1500 RCF at 4 °C for 5 min and the supernatant was discarded. The cell pellet was suspended in 1 ml TRIzol, vortexed, and promptly stored at -80 °C until RNA extractions. Cells were lysed using FastPrep homogenizer with bead beating in TRIzol. Lysate was cleaned up using a Zymo kit with on column DNase treatment, and RNA was eluted in 30 µl of kit-provided water. cDNA libraries were then generated using a Thermo Fisher/Invitrogen SuperScript™ IV First-Strand Synthesis System (Catalog #18091200). cDNA, PowerSybr Green (Thermo Fisher: 4368706), and primers were mixed in triplicate in a MicroAmp™ Fast Optical 96-Well Reaction Plate with Barcode (Catalog #4346906) and sealed with an optical adhesive cover (Catalog #4360954). Primer sequences were as follows: GAPDH (JGI ID: 53883): forward TGGCTCCAATTGCTGCTGTTT, reverse CCTAGCAGCACCAGTTGAAGA; G protein (77952): forward ACGGTTGGGTCACTTGTGTTTGTCC, reverse GAGCGTGACCAGTGAGGGATC; mitotic α-tubulin (58607): forward GGTCTTGTATGTGTGCCGAAC, reverse TTAGCAGCATCTTCACGACCAGT; mitotic α-tubulin (55745) forward CACACACAAAATGAGAGAAGTCGTC, reverse TTCCATGTTCAGCACAGAATAATTC; mitotic β-tubulin (55748): forward AACCAACACTGCTTCTCCACTCG, reverse TCTGGACGGAATAATTGACCTTGG; mitotic β-tubulin (55900): forward GGTTGCTGGTGTCTGCTGGTG, reverse GCAGCCAAAGGAGCAGAACCAA. Samples were run on a StepOne Real-Time PCR machine and analyzed using StepOne software v2.3.

The fold change in mRNA abundance was determined from C<sub>T</sub> values using the 2<sup>-ΔΔC<sub>T</sub></sup> method (Livak and Schmittgen, 2001). Using this method, the flask that remained at 30 °C was a time-matched control for the experimental flask at the time point before the temperature shift, and the time point after the shift to 38 °C. A *Naegleria* G protein was used as the housekeeping gene to normalize the data, and a second housekeeping gene (GAPDH) was used to verify the results.

The microarray data in **Fig. 1D** was originally acquired in (Fritz-Laylin and Cande, 2010). Each experimental replicate had been completed with 2 technical replicates, so the technical

replicates were first averaged. Then, the mRNA abundance at the 0 min time point (before differentiation) and at the 80 min time point (after differentiation to flagellates) were compared for each biological replicate to calculate the fold change in mRNA abundance for mitotic and flagellate tubulins.

**Immunofluorescence:** Immunofluorescence staining of amoebae and flagellates in Fig 1B was performed using an actin cytoskeleton fixation protocol modified from (Velle and Fritz-Laylin, 2020). Cells were taken from an edge plate or from a sample of differentiated cells (see above), spun down at 1500 RCF for 90 sec, and cell pellets were resuspended in 1.5 ml 2 mM Tris. Cells were fixed in an equal volume of 2x fixative (50 mM sodium phosphate buffer, 125 mM sucrose, and 3.6% paraformaldehyde) for 15 minutes, then transferred to a 96 well glass-bottom plate coated with 0.1% poly(ethyleneimine) and allowed to settle for 15 min. Cells were rinsed twice in PEM (100 mM PIPES, 1 mM EGTA, 0.1 mM MgSO<sub>4</sub>; pH ~7.4) and permeabilized for 10 min in PEM + 0.1% NP-40 Alternative (Millipore, 492016) + 6.6 nM Alexa Fluor™ 488 Phalloidin (and 0.2x Tubulin Tracker Deep Red (Life Technologies, T34077, prepared according to manufacturer instructions) columns 1, 2 and 4 only). Cells were rinsed twice in PEM, then blocked in PEMBALG (PEM + 1% BSA, 0.1% sodium azide, 100 mM lysine, and 0.5% cold fish water gelatin; pH 7.4) at room temperature for 1 h. Cells were then incubated in primary antibody (anti- $\alpha$ -tubulin mouse monoclonal antibody (clone DM1A), Sigma, T6199) diluted to ~10  $\mu$ g/ml in PEMBALG for 1 h. Cells were washed 3 times in PEMBALG, then incubated at room temperature for 1 h in Alexa Fluor™ 555 conjugated goat anti-mouse secondary antibody (Life Technologies, A21424) diluted to 2  $\mu$ g/ml in PEMBALG, with 1x Tubulin Tracker Deep Red, ~66 nM Alexa Fluor™ 488 Phalloidin, and 1  $\mu$ g/ml DAPI. Cells were then rinsed 4 times in PEM, and imaged the same day.

Immunofluorescence staining in the remaining figures was optimized for microtubules and performed using amoeba from a fresh edge plate that had grown about half-way across the dish (or from a mitotic synchrony, detailed above). Cells were removed from the plate and added to approximately 3 mls of water in a conical tube, spun down in a clinical centrifuge at setting 7 for ~40 seconds and the supernatant removed leaving ~500  $\mu$ l of water above the cell pellet. To this mixture an equal volume of freshly prepared 2X fixative solution consisting of 2 mM Tris pH 7.2; 125 mM sucrose; 10 mM NaCl, 2% paraformaldehyde was added and mixed gently. Cells were fixed for 10 min at room temperature. Cells were then placed on freshly coated coverslips and allowed to adhere for approximately 20-30 minutes. Coverslips were plasma cleaned and then coated with 0.1% poly(ethyleneimine). After cells were adhered to the coverslips, they were rinsed 3 times with 1 ml of PEM (100 mM PIPES, pH 6.9; 1 mM EGTA; 0.1 mM MgSO<sub>4</sub>) and then permeabilized with 0.1% NP-40 for 10 minutes. Cells were blocked in PEM-BALG (PEM buffer supplemented with 1% BSA, 100 mM lysine, and 0.5% cold fish water gelatin) for one hour or overnight and then incubated with primary antibody for 1 hour at 37 °C or at room temperature overnight. Coverslips were rinsed in PBS containing 0.1% Tween and 0.02% sodium azide and incubated with Dylight-488 labeled anti-mouse secondary antibodies (Invitrogen) according to the manufacturers' recommended protocol. Finally, coverslips were washed in PEM supplemented with 0.01% Triton-X-100 for 5 minutes before mounting on clean slides using DAPI Fluoromount G (Southern Biotech) or Prolong Gold.

**Confocal imaging:** Cells were imaged on a Nikon Ti-E microscope with a CSU-X1 Yokogawa spinning-disk confocal scan head (PerkinElmer, Wellesley, MA), an Andor iXon+ electron-multiplying charge-coupled device camera (Andor), using a 100X/1.4 NA objective lens.



556 Z-step size was set at 0.2  $\mu\text{m}$ .

557 Laser powers and exposures were chosen to ensure that the fluorescent signal would not be  
558 saturated and were adjusted depending on the fluorescent signal. For imaging microtubules with  
559 a Dylight 488 labeled secondary antibody, images were acquired using a 488 nm laser at 10.2%  
560 power; for imaging DNA, the 405 nm laser was used at 40.2% power.

561 The images in Fig. 1B were taken on a Nikon Ti2 microscope equipped with a Plan Apo  $\lambda$  100x  
562 oil objective (1.45 NA), a Crest spinning disk (50  $\mu\text{m}$ ), a Prime 95B CMOS camera, and a  
563 Spectra III/Celesta light source (at 50-60% power with excitation wavelengths of 477, 546, and  
564 638 nm). The microscope was controlled through NIS Elements software, and images were  
565 acquired as multi-channel z stacks with a step size of 200 nm and exposures of 200 ms (to  
566 image fluorescent phalloidin and tubulin antibody staining) or 500 ms (to image tubulin tracker  
567 staining).

568 **Digital deconvolution and 3D reconstructions:** Z stacks captured using a spinning disk  
569 confocal microscope were digitally deconvolved using Autoquant X3 software. The default 3D  
570 deconvolution settings for spinning disk confocal data were used with “expert recommended  
571 settings,” and 40 iterations. The deconvolved images were then processed in Fiji (Schindelin *et*  
572 *al.*, 2012) to set the scaling, and to remove the mitochondria prior to 3D rendering, as the  
573 intensely-stained mitochondria made it difficult to observe the DNA in the nucleus. The resulting  
574 deconvolved image stacks were used to generate 3D surface renderings in UCSF ChimeraX  
575 software (Pettersen *et al.*, 2021).

576 **Analysis of spindle morphology:** Spindle length and width measurements were assessed  
577 using the raw confocal (not deconvolved) datasets, and were only measured for spindles lying  
578 parallel to the plane of the coverslip. Length was measured by drawing a line in Fiji using the  
579 straight line tool, and measuring from the end of one pole to the opposite pole. For spindles in  
580 prophase where the poles are unclear, the longest axis was measured. In cases where the  
581 spindle bent during telophase (e.g. **Fig. 3A**, Anaphase/Telophase), the segmented line tool was  
582 used to follow the length of the spindle more accurately. Spindle width was measured using only  
583 the straight line tool, and was assessed at the approximate midpoint of the spindle between the  
584 two poles. These length and width values were separated by spindle stage, and were plotted  
585 using GraphPad Prism 8 software.

586 The number of bundles and the distance between bundles were calculated from confocal  
587 Z-stacks of metaphase spindles lying perpendicular to the coverslip. Bundle number was  
588 assessed in each plane going through the bundle for 8 representative spindles (**Fig. 4B**), and  
589 the maximum number of bundles present at the midplane was calculated for additional  
590 metaphase spindles. To determine the average distance between bundles, a frame that  
591 represented the spindle midplane was used, and the center of each bundle was selected using  
592 the multi-point tool in Fiji. The coordinates of each bundle center were used to determine the  
593 distance from each bundle to its two nearest neighboring bundles.

594 Line scan analysis (**Fig. 4D**, **Fig. S6**) was completed using confocal images of spindles that  
595 were oriented parallel to the coverslip. Image stacks were first transformed into sum intensity  
596 projections in Fiji. Then, the line width was matched to the width of the spindle, and a line (or  
597 segmented line in the case of bent anaphase/telophase spindles) was drawn to include the



entire spindle length, with a short length of background at each end. The “plot profile” tool in Fiji was then used to extract the average pixel intensity along the line for tubulin and DNA staining. These values were normalized to the average intensity of an area of the cell adjacent to the spindle, which was set to 1. The spindle lengths were also normalized such that “0” represents the midpoint of the spindle. To determine the relative quantity of DNA and tubulin in these spindles (**Fig. 4E**), the area under the linescan-generated curves was calculated using GraphPad Prism 8 software, using a baseline level of 1.

**Analysis of spindle twist:** To characterize the shape of microtubule bundles, we manually tracked individual bundles of vertically oriented spindles, and horizontally oriented spindles whose image stacks were first transformed into vertical (end-on) orientation, using Multipoint tool in Fiji. As microtubule bundles appear as spots in a spindle cross-section, each point was placed at the center of the signal and its x,y,z coordinates were saved. Moving up and down through the z-stack helped to determine this point. Each bundle was tracked through all z-planes where it was visible. Positions of the spindle poles were also determined, as the spots in the center of the end points of all bundles in the plane beyond the bundle ends. Coordinates of bundles and poles were transformed so that both poles are on the z-axis.

To describe the shape of a microtubule bundle, we fit a plane to the points representing the bundle. Subsequently, we fit a circle that lies in this plane to the same points. These fits were used to calculate the curvature and twist of the bundle as follows: (i) The curvature is calculated as one over the radius, and (ii) the twist is calculated as the angle between the plane and the z-axis divided by the mean distance of these points from the z-axis. Bundle length was calculated as the length of the projection of the bundle trace onto the pole-to-pole axis. For detailed descriptions of this method, see (Ivec *et al.*, 2021).

**Transmission Electron Microscopy:** Cells were fixed overnight at 4 °C in 2.5% glutaraldehyde + 100 mM sodium cacodylate, then rinsed and stored in 100 mM sodium cacodylate overnight. Samples were then rinsed in 100 mM sodium cacodylate buffer, pH 7.4, three times for 10 minutes per wash. Cells were post fixed in 1% aqueous osmium tetroxide (Electron Microscopy Sciences) in 100 mM sodium cacodylate buffer overnight at 4 °C. Cells were then rinsed twice in water for 10 min per wash, before en bloc staining with 1% uranyl acetate (Electron Microscopy Sciences) in water for 1 hour at room temperature. Cells were rinsed 3 times in water, for 10 min per wash. Cells were then subjected to a graded ethanol dehydration series as follows with 15 min washes at each of the following ethanol concentrations: 50%, 70%, 80%, 90%, 95%, followed by two ten minute washes in 100% ethanol. Cells were quickly rinsed in propylene oxide, then infiltrated with 50% resin (Araldite 502/Embed-12, Electron Microscopy Sciences) and propylene oxide overnight. Cells were then incubated for 6-12 hours in each of the following resin concentrations: 70%, 85%, 95%, and 100% followed by embedding in 100% resin at 60 °C for 4 days. ~70 nm thin sections were cut using an RMC PowerTime XL Ultramicrotome with a Diatome diamond knife, and were transferred to copper grids. Sections were post stained with 1% uranyl acetate for 6 min, and lead citrate for 2 min. Images were taken using a JEOL JEM-200CX transmission electron microscope.

## 638 ACKNOWLEDGEMENTS

639 We thank Nenad Pavin for discussions about the analysis of spindle twist, Shane Hussey for  
640 assistance with sequence analysis, Joshua Rafferty and Shadi Mahjoun for technical  
641 assistance, Laura Katz (Smith College) for assistance with the PhyloToL pipeline, and Sandra  
642 Balduaf (Uppsala University) for *Acrasis* tubulin sequences. We thank Chandler Fulton  
643 (Brandeis University) for strains and advice. We thank Alfredo Guzman for designing primers,  
644 Ravi Ranjan (University of Massachusetts, Genomics Resource Laboratory) for RNA  
645 extractions, and Madelaine Bartlett (UMass) and Courtney Babbitt (UMass) for qPCR  
646 equipment. We thank Andrew Kennard (UMass) and Tom Maresca (UMass) for comments on  
647 the manuscript. Light microscopy data was gathered in the Light Microscopy Facility and Nikon  
648 Center of Excellence at the Institute for Applied Life Sciences, UMass Amherst. We thank Kasia  
649 Hammar (Marine Biological Laboratory) for assistance with Transmission Electron Microscopy.  
650 3D reconstructions were generated in UCSF ChimeraX, developed by the Resource for  
651 Biocomputing, Visualization, and Informatics at the University of California, San Francisco, with  
652 support from National Institutes of Health R01-GM129325 and the Office of Cyber Infrastructure  
653 and Computational Biology, National Institute of Allergy and Infectious Diseases. This work was  
654 supported by the National Institute Of Allergy And Infectious Diseases of the National Institutes  
655 of Health under Award Number F32AI150057 to K.B.V. and Award Number 1R21AI139363 to  
656 L.K.F.-L., and a Smith Family Foundation Award for Excellence in Biomedical Science to  
657 L.K.F.-L. The work of doctoral students M.T. and A.I. has been supported by the “Young  
658 researchers' career development project – training of doctoral students” of the Croatian Science  
659 Foundation. M.T., A.I. and I.M.T. acknowledge the support of the European Research Council  
660 (ERC Consolidator Grant, GA Number 647077) and the Croatian Science Foundation (HRZZ  
661 project IP2019-04-5967). Work in L.M.R.'s lab was supported by the NSF (MCB-1615938 and  
662 MCB-2017687) and the Robert A Welch Foundation (I-1908).

## 663 REFERENCES

- 664 Akiyoshi, B. and Gull, K. (2014) 'Discovery of unconventional kinetochores in kinetoplastids',  
665 *Cell*, 156(6), pp. 1247–1258.
- 666 Alushin, G. M. *et al.* (2014) 'High-resolution microtubule structures reveal the structural  
667 transitions in  $\alpha\beta$ -tubulin upon GTP hydrolysis', *Cell*, 157(5), pp. 1117–1129.
- 668 Anisimova, M. *et al.* (2011) 'Survey of branch support methods demonstrates accuracy, power,  
669 and robustness of fast likelihood-based approximation schemes', *Systematic biology*, 60(5), pp.  
670 685–699.
- 671 Brunet, S. *et al.* (1999) 'Kinetochore fibers are not involved in the formation of the first meiotic  
672 spindle in mouse oocytes, but control the exit from the first meiotic M phase', *The Journal of cell*  
673 *biology*, 146(1), pp. 1–12.
- 674 Cerón-Romero, M. A. *et al.* (2019) 'PhyloToL: A Taxon/Gene-Rich Phylogenomic Pipeline to  
675 Explore Genome Evolution of Diverse Eukaryotes', *Molecular biology and evolution*, 36(8), pp.  
676 1831–1842.
- 677 Chung, S. *et al.* (2002) 'Cloning and characterization of a divergent alpha-tubulin that is  
678 expressed specifically in dividing amebae of *Naegleria gruberi*', *Gene*, 293(1-2), pp. 77–86.
- 679 Danlasky, B. M. *et al.* (2020) 'Evidence for anaphase pulling forces during *C. elegans* meiosis',  
680 *The Journal of cell biology*, 219(12). doi: 10.1083/jcb.202005179.
- 681 D'Archivio, S. and Wickstead, B. (2017) 'Trypanosome outer kinetochore proteins suggest  
682 conservation of chromosome segregation machinery across eukaryotes', *The Journal of cell*  
683 *biology*, 216(2), pp. 379–391.
- 684 Drinnenberg, I. A. and Akiyoshi, B. (2017) 'Evolutionary Lessons from Species with Unique  
685 Kinetochores', *Progress in molecular and subcellular biology*, 56, pp. 111–138.
- 686 Dumont, J., Oegema, K. and Desai, A. (2010) 'A kinetochore-independent mechanism drives  
687 anaphase chromosome separation during acentrosomal meiosis', *Nature cell biology*, 12(9), pp.  
688 894–901.
- 689 Eshun-Wilson, L. *et al.* (2019) 'Effects of  $\alpha$ -tubulin acetylation on microtubule structure and  
690 stability', *Proceedings of the National Academy of Sciences of the United States of America*,  
691 116(21), pp. 10366–10371.
- 692 Fritz-Laylin, L. K., Assaf, Z. J., *et al.* (2010) '*Naegleria gruberi* de novo basal body assembly  
693 occurs via stepwise incorporation of conserved proteins', *Eukaryotic cell*, 9(6), pp. 860–865.
- 694 Fritz-Laylin, L. K., Prochnik, S. E., *et al.* (2010) 'The genome of *Naegleria gruberi* illuminates  
695 early eukaryotic versatility', *Cell*, 140(5), pp. 631–642.
- 696 Fritz-Laylin, L. K. *et al.* (2011) 'The *Naegleria* genome: a free-living microbial eukaryote lends  
697 unique insights into core eukaryotic cell biology', *Research in microbiology*, 162(6), pp.  
698 607–618.

699 Fritz-Laylin, L. K. and Cande, W. Z. (2010) 'Ancestral centriole and flagella proteins identified by  
700 analysis of *Naegleria* differentiation', *Journal of cell science*, 123(Pt 23), pp. 4024–4031.

701 Fulton, C. (1983) 'Macromolecular syntheses during the quick-change act of *Naegleria*', *The*  
702 *Journal of protozoology*, 30(2), pp. 192–198.

703 Fulton, C. (1993) 'Naegleria: A Research Partner For Cell and Developmental Biology 1', *The*  
704 *Journal of eukaryotic microbiology*, 40(4), pp. 520–532.

705 Fulton, C. and Dingle, A. D. (1971) 'Basal bodies, but not centrioles, in *Naegleria*', *The Journal*  
706 *of cell biology*, 51(3), pp. 826–836.

707 Fulton, C. and Guerrini, A. M. (1969) 'Mitotic synchrony in *Naegleria amebae*', *Experimental cell*  
708 *research*, 56(2), pp. 194–200.

709 Fulton, C. and Kowit, J. D. (1975) 'Programmed synthesis of flagellar tubulin during cell  
710 differentiation in *Naegleria*', *Annals of the New York Academy of Sciences*, 253, pp. 318–332.

711 Fulton, C. and Simpson, P. A. (1976) 'Selective synthesis and utilization of flagellar tubulin. The  
712 multi-tubulin hypothesis', *Cell motility*, 3, pp. 987–1005.

713 González-Robles, A. *et al.* (2009) '*Naegleria fowleri*: light and electron microscopy study of  
714 mitosis', *Experimental parasitology*, 122(3), pp. 212–217.

715 Guindon, S. *et al.* (2010) 'New algorithms and methods to estimate maximum-likelihood  
716 phylogenies: assessing the performance of PhyML 3.0', *Systematic biology*, 59(3), pp. 307–321.

717 Gupta, M. L., Jr *et al.* (2003) 'Understanding tubulin-Taxol interactions: mutations that impart  
718 Taxol binding to yeast tubulin', *Proceedings of the National Academy of Sciences of the United*  
719 *States of America*, 100(11), pp. 6394–6397.

720 Heald, R. *et al.* (1996) 'Self-organization of microtubules into bipolar spindles around artificial  
721 chromosomes in *Xenopus* egg extracts', *Nature*, 382(6590), pp. 420–425.

722 Herman, E. K. *et al.* (2020) 'A comparative 'omics approach to candidate pathogenicity factor  
723 discovery in the brain-eating amoeba *Naegleria fowleri*', *bioRxiv*. bioRxiv. doi:  
724 10.1101/2020.01.16.908186.

725 Heuser, M. and Razavi, L. (1970) 'Chapter 13 Amebo-flagellates as Research Partners: The  
726 Laboratory Biology of *Naegleria* and *Tetramitus*', in Prescott, D. M. (ed.) *Methods in Cell*  
727 *Biology*. Academic Press, pp. 341–476.

728 Hoang, D. T. *et al.* (2018) 'UFBoot2: Improving the Ultrafast Bootstrap Approximation',  
729 *Molecular biology and evolution*, 35(2), pp. 518–522.

730 van Hooff, J. J. *et al.* (2017) 'Evolutionary dynamics of the kinetochore network in eukaryotes as  
731 revealed by comparative genomics', *EMBO reports*, 18(9), pp. 1559–1571.

732 Hoyle, H. D. and Raff, E. C. (1990) 'Two *Drosophila* beta tubulin isoforms are not functionally  
733 equivalent', *The Journal of cell biology*, 111(3), pp. 1009–1026.

734 Inoué, S. and Salmon, E. D. (1995) 'Force generation by microtubule assembly/disassembly in  
735 mitosis and related movements', *Molecular biology of the cell*, 6(12), pp. 1619–1640.

736 Ivec, A. *et al.* (2021) 'Measurement of curvature and twist of microtubule bundles in the mitotic  
737 spindle', *bioRxiv*. doi: 10.1101/2021.01.02.425081.

738 Johnson, K. A. (1998) 'The axonemal microtubules of the Chlamydomonas flagellum differ in  
739 tubulin isoform content', *Journal of cell science*, 111 ( Pt 3), pp. 313–320.

740 Kajtez, J. *et al.* (2016) 'Overlap microtubules link sister k-fibres and balance the forces on  
741 bi-oriented kinetochores', *Nature communications*, 7, p. 10298.

742 Kalyaanamoorthy, S. *et al.* (2017) 'ModelFinder: fast model selection for accurate phylogenetic  
743 estimates', *Nature methods*, 14(6), pp. 587–589.

744 Kapoor, T. M. *et al.* (2006) 'Chromosomes can congress to the metaphase plate before  
745 biorientation', *Science*, 311(5759), pp. 388–391.

746 Kowit, J. D. and Fulton, C. (1974a) 'Programmed synthesis of tubulin for the flagella that  
747 develop during cell differentiation in Naegleria gruberi', *Proceedings of the National Academy of  
748 Sciences of the United States of America*, 71(7), pp. 2877–2881.

749 Kowit, J. D. and Fulton, C. (1974b) 'Purification and properties of flagellar outer doublet tubulin  
750 from Naegleria gruberi and a radioimmune assay for tubulin', *The Journal of biological  
751 chemistry*, 249(11), pp. 3638–3646.

752 Lai, E. Y. *et al.* (1979) 'Programmed appearance of translatable flagellar tubulin mRNA during  
753 cell differentiation in Naegleria', *Cell*, 17(4), pp. 867–878.

754 Lai, E. Y., Remillard, S. P. and Fulton, C. (1988) 'The alpha-tubulin gene family expressed  
755 during cell differentiation in Naegleria gruberi', *The Journal of cell biology*, 106(6), pp.  
756 2035–2046.

757 Lee, J. H. and Walsh, C. J. (1988) 'Transcriptional regulation of coordinate changes in flagellar  
758 mRNAs during differentiation of Naegleria gruberi amebae into flagellates', *Molecular and  
759 cellular biology*, 8(6), pp. 2280–2287.

760 Letunic, I. and Bork, P. (2019) 'Interactive Tree Of Life (iTOL) v4: recent updates and new  
761 developments', *Nucleic acids research*. doi: 10.1093/nar/gkz239.

762 Livak, K. J. and Schmittgen, T. D. (2001) 'Analysis of relative gene expression data using  
763 real-time quantitative PCR and the 2(-Delta Delta C(T)) Method', *Methods*, 25(4), pp. 402–408.

764 Madeira, F. *et al.* (2019) 'The EMBL-EBI search and sequence analysis tools APIs in 2019',  
765 *Nucleic acids research*, 47(W1), pp. W636–W641.

766 Manenica, M. *et al.* (2020) 'Augmin regulates kinetochore tension and spatial arrangement of  
767 spindle microtubules by nucleating bridging fibers', *bioRxiv*. doi: 10.1101/2020.09.10.291740.

768 Mastronarde, D. N. *et al.* (1993) 'Interpolar spindle microtubules in PTK cells', *The Journal of*



769 *cell biology*, 123(6 Pt 1), pp. 1475–1489.

770 Matthews, K. A., Rees, D. and Kaufman, T. C. (1993) 'A functionally specialized alpha-tubulin is  
771 required for oocyte meiosis and cleavage mitoses in *Drosophila*', *Development*, 117(3), pp.  
772 977–991.

773 McIntosh, J. R., Molodtsov, M. I. and Ataullakhanov, F. I. (2012) 'Biophysics of mitosis',  
774 *Quarterly reviews of biophysics*, 45(2), pp. 147–207.

775 Meza, I., Talamás-Rohana, P. and Vargas, M. A. (2006) 'The cytoskeleton of *Entamoeba*  
776 *histolytica*: structure, function, and regulation by signaling pathways', *Archives of medical*  
777 *research*, 37(2), pp. 234–243.

778 Minh, B. Q. *et al.* (2020) 'IQ-TREE 2: New Models and Efficient Methods for Phylogenetic  
779 Inference in the Genomic Era', *Molecular biology and evolution*, 37(5), pp. 1530–1534.

780 Mirarab, S. *et al.* (2015) 'PASTA: Ultra-Large Multiple Sequence Alignment for Nucleotide and  
781 Amino-Acid Sequences', *Journal of computational biology: a journal of computational molecular*  
782 *cell biology*, 22(5), pp. 377–386.

783 Mullen, T. J., Davis-Roca, A. C. and Wignall, S. M. (2019) 'Spindle assembly and chromosome  
784 dynamics during oocyte meiosis', *Current opinion in cell biology*, 60, pp. 53–59.

785 Novak, M. *et al.* (2018) 'The mitotic spindle is chiral due to torques within microtubule bundles',  
786 *Nature communications*, 9(1), p. 3571.

787 Pei, J. and Grishin, N. V. (2001) 'AL2CO: calculation of positional conservation in a protein  
788 sequence alignment', *Bioinformatics*, 17(8), pp. 700–712.

789 Pettersen, E. F. *et al.* (2021) 'UCSF ChimeraX: Structure visualization for researchers,  
790 educators, and developers', *Protein science: a publication of the Protein Society*, 30(1), pp.  
791 70–82.

792 Raff, E. C. (1984) 'Genetics of microtubule systems', *The Journal of cell biology*, 99(1 Pt 1), pp.  
793 1–10.

794 Savage, C. *et al.* (1989) 'mec-7 is a beta-tubulin gene required for the production of  
795 15-protofilament microtubules in *Caenorhabditis elegans*', *Genes & development*, 3(6), pp.  
796 870–881.

797 Schindelin, J. *et al.* (2012) 'Fiji: an open-source platform for biological-image analysis', *Nature*  
798 *methods*, 9(7), pp. 676–682.

799 Siddiqui, R. *et al.* (2016) 'Biology and pathogenesis of *Naegleria fowleri*', *Acta tropica*, 164, pp.  
800 375–394.

801 Simunić, J. and Tolić, I. M. (2016) 'Mitotic Spindle Assembly: Building the Bridge between Sister  
802 K-Fibers', *Trends in biochemical sciences*, 41(10), pp. 824–833.

803 Tolić, I. M., Novak, M. and Pavin, N. (2019) 'Helical Twist and Rotational Forces in the Mitotic

- 804 Spindle', *Biomolecules*, 9(4). doi: 10.3390/biom9040132.
- 805 Velle, K. B. and Fritz-Laylin, L. K. (2020) 'Conserved actin machinery drives  
806 microtubule-independent motility and phagocytosis in *Naegleria*', *The Journal of cell biology*,  
807 219(11). doi: 10.1083/jcb.202007158.
- 808 Vemu, A. *et al.* (2017) 'Tubulin isoform composition tunes microtubule dynamics', *Molecular*  
809 *biology of the cell*, 28(25), pp. 3564–3572.
- 810 Vukušić, K. *et al.* (2017) 'Microtubule Sliding within the Bridging Fiber Pushes Kinetochore  
811 Fibers Apart to Segregate Chromosomes', *Developmental cell*, 43(1), pp. 11–23.e6.
- 812 Vukušić, K., Buđa, R. and Tolić, I. M. (2019) 'Force-generating mechanisms of anaphase in  
813 human cells', *Journal of cell science*, 132(18). doi: 10.1242/jcs.231985.
- 814 Walsh, C. J. (2007) 'The role of actin, actomyosin and microtubules in defining cell shape during  
815 the differentiation of *Naegleria amebae* into flagellates', *European journal of cell biology*, 86(2),  
816 pp. 85–98.
- 817 Walsh, C. J. (2012) 'The structure of the mitotic spindle and nucleolus during mitosis in the  
818 amebo-flagellate *Naegleria*', *PloS one*, 7(4), p. e34763.
- 819 Wilson, P. G. and Borisy, G. G. (1997) 'Evolution of the multi-tubulin hypothesis', *BioEssays:*  
820 *news and reviews in molecular, cellular and developmental biology*, 19(6), pp. 451–454.

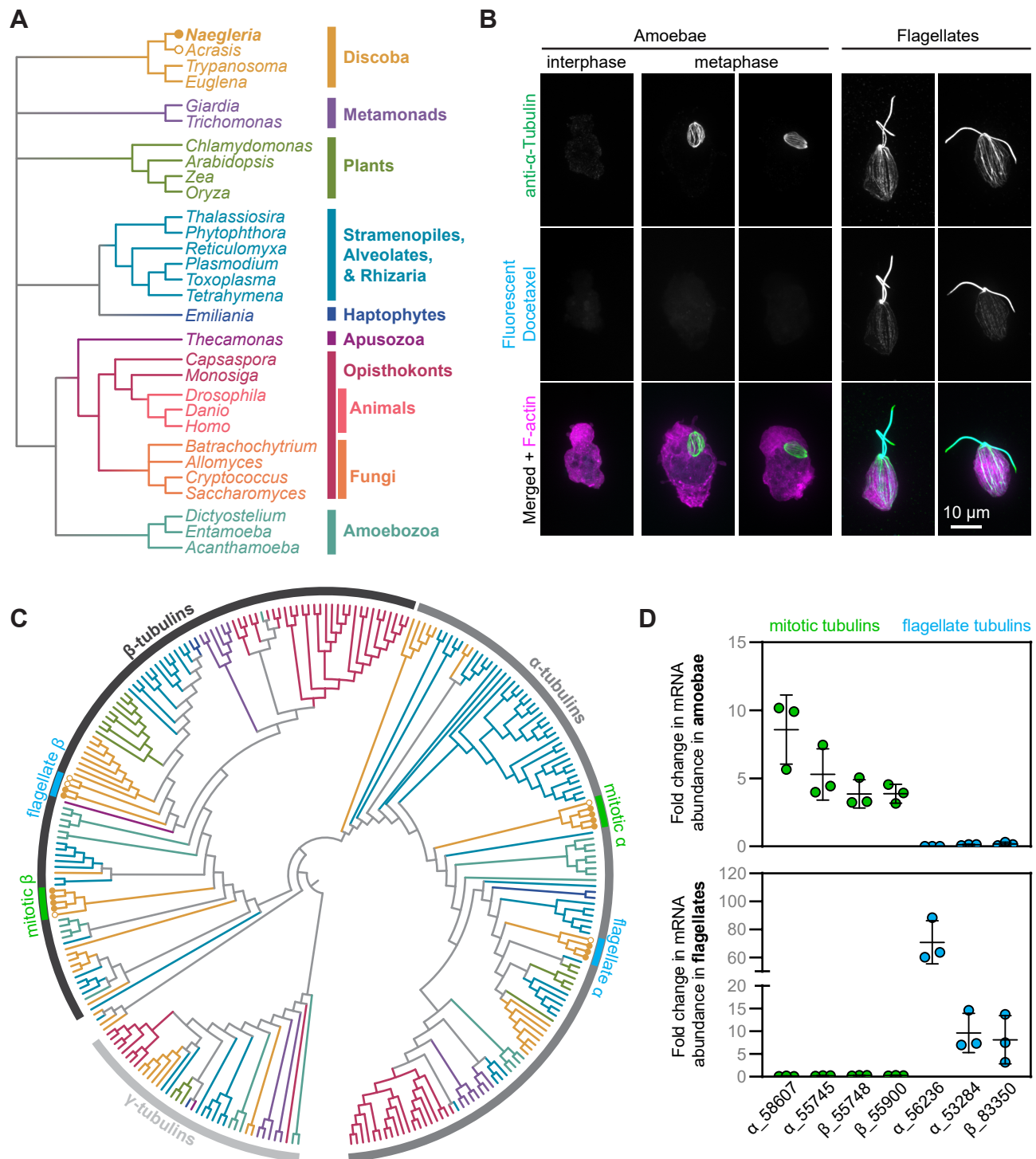


**Figure 1. *Naegleria* has flagellate and mitotic microtubule arrays composed of distinct tubulins.** (A) The evolutionary relationships between *Naegleria* and other eukaryotes are shown using a cladogram (branch lengths are meaningless) modified from Velle and Fritz-Laylin, 2019. (B) Amoebae from a growing population (left), or flagellates from a differentiated population (right), were fixed and stained with antibodies (anti-alpha tubulin clone DM1A, green) and Tubulin Tracker (Fluorescent Docetaxel, cyan) to detect microtubules, and Alexa Fluor 488 conjugated Phalloidin to label F-actin (magenta). Maximum intensity projections of cells are shown. (C) The evolutionary relationship of gamma, alpha, and beta tubulins from the species in panel A are shown using a cladogram (using the color scheme from A, see Fig. S1 for the full tree). The tree is rooted on gamma tubulins, and shows mitotic (green) and flagellate (blue) tubulins from *Naegleria* (closed circles) and *Acrasis* (open circles). (D) The fold changes in tubulin mRNA in amoebae compared to flagellates (top) or flagellates compared to amoebae (bottom) were calculated from data reported in Fritz-Laylin and Cande, 2010. Each point represents one experimental replicate, and lines denote the average  $\pm$  standard deviation (SD). Tubulins are labeled with JGI identification numbers.

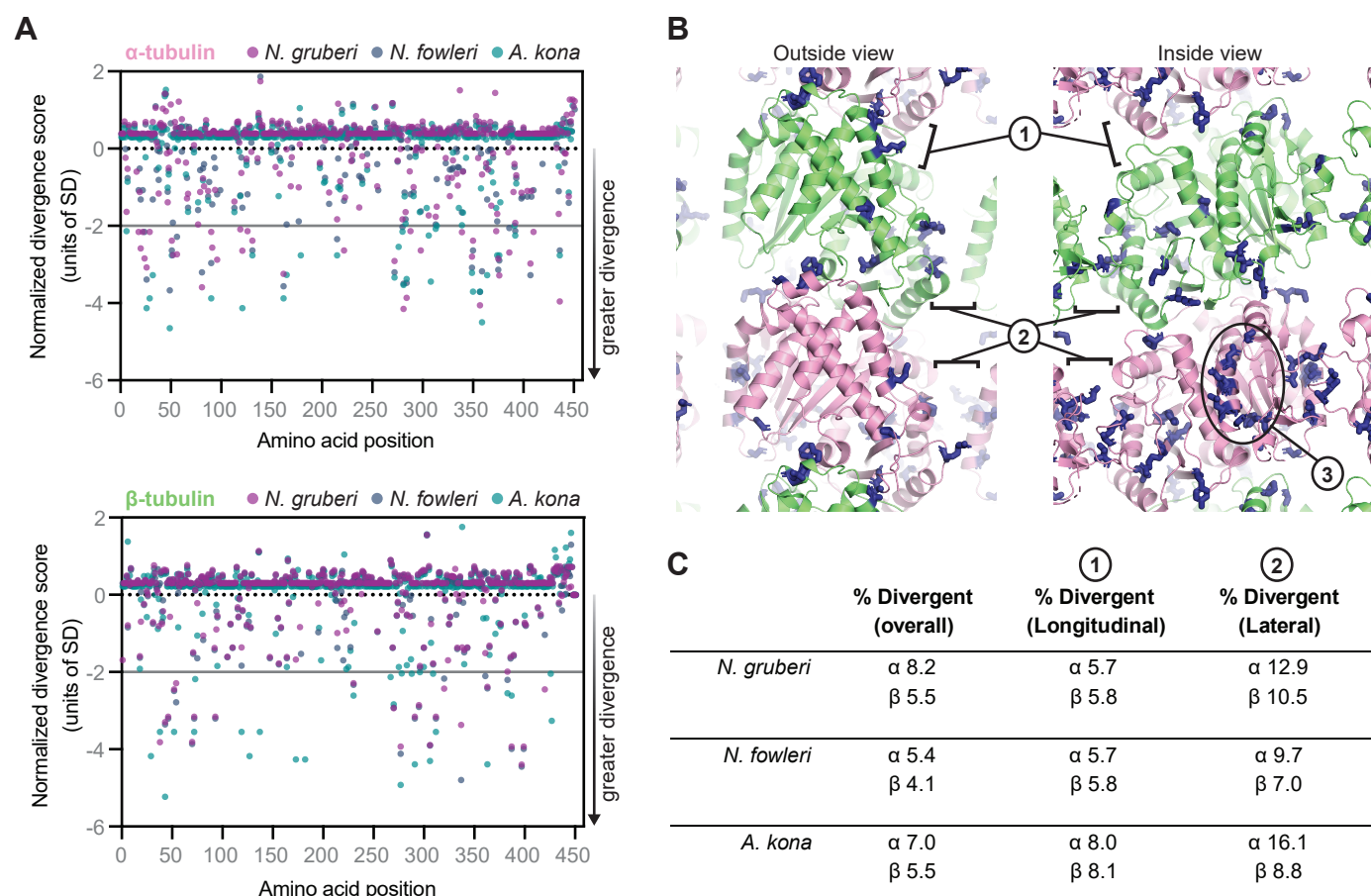


**Figure 2. Comparative analysis of evolutionary divergence for mitotic and flagellate tubulins.** (A) Plots of the normalized divergence score (see Methods) as a function of amino acid position for  $\alpha$ -tubulin (top) and  $\beta$ -tubulin (bottom). Lower scores indicate positions where mitotic tubulins show increased divergence relative to flagellate tubulins. The analysis was performed on three species: *N. gruberi* (lavender), *N. fowleri* (navy), and *A. kona* (teal). The horizontal gray line indicates the two standard deviation cutoff we used to identify especially divergent sites. (B) Structural context of the sites with increased divergence in the mitotic tubulins. Side-chain positions for the *N. gruberi* amino acids identified in (A) are represented as sticks (blue) on a model of  $\alpha\beta$ -tubulin in the microtubule lattice ( $\alpha$ -tubulin: pink,  $\beta$ -tubulin: lime). 'Outside' and 'Inside' views of the lattice are shown, and longitudinal (labeled 1) and lateral (labeled 2) microtubule lattice contacts are indicated, as is the luminal (internal) surface of  $\alpha$ -tubulin (labeled 3). (C) Table summarizing the proportion of positions with elevated divergence near microtubule lattice interfaces. For all three species, there are more divergent positions in  $\alpha$ -tubulin compared to  $\beta$ -tubulin, and the divergence seems to be particularly enriched at the lateral interfaces. See Fig. S4 for details.



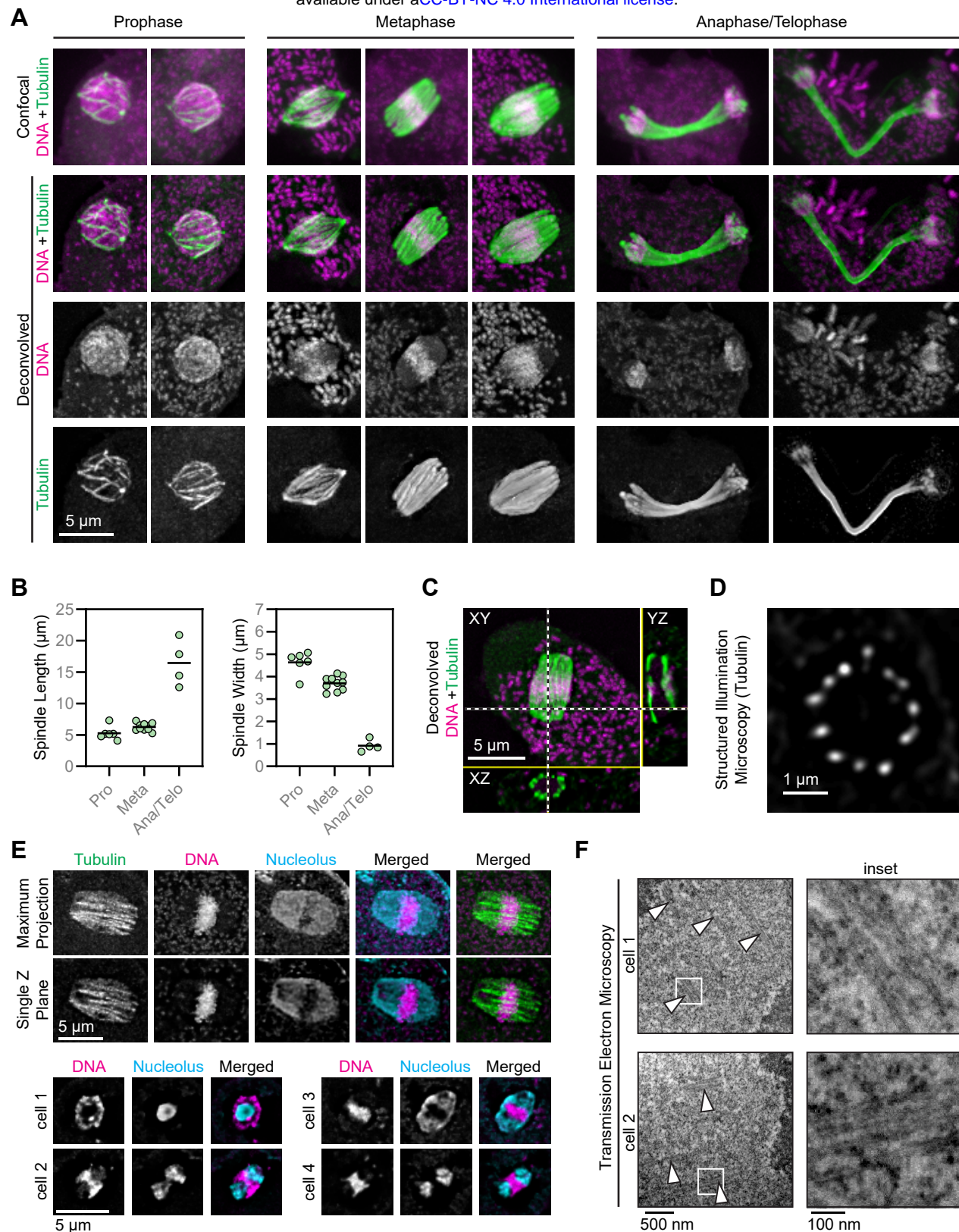


**Figure 3. *Naegleria*'s spindle is a barrel shape composed of bundles of microtubules that elongate as mitosis proceeds.** (A) Asynchronously growing *Naegleria* amoebae were fixed and stained with anti-alpha tubulin clone DM1A (green) to detect microtubules, and DAPI to label DNA (magenta). Mitotic spindles were imaged using confocal microscopy (top row), and images were deconvolved using Autoquant software (bottom rows). Cells were classified as prophase, metaphase, or anaphase/telophase. (B) Quantification of maximum spindle length (left) and the spindle width at half the length (right). Each point represents one mitotic spindle, and lines indicate the averages (prophase, n=6; metaphase, n=10; anaphase/telophase, n=4). Spindles imaged and deconvolved as in (A). (C)



Orthogonal views of a metaphase spindle (imaged and deconvolved as in A) lying in the plane of the coverslip; XZ and YZ views generated in Fiji. **(D)** Structured illumination microscopy of a spindle lying perpendicular to the coverslip. **(E)** Confocal microscopy and deconvolution of nucleoli in mitotic *Naegleria*. Cells were fixed and stained to detect tubulin (YOL 1/34 antibody, green, top panels only), DNA (DAPI, magenta), and nucleolar protein (DE6 antibody, cyan). One maximum intensity projection is shown (top cell), while remaining images are single Z planes. **(F)** Transmission electron microscopy of microtubule bundles in *Naegleria*; arrowheads indicate microtubule bundles and boxed regions (left) are shown as enlarged insets (right).

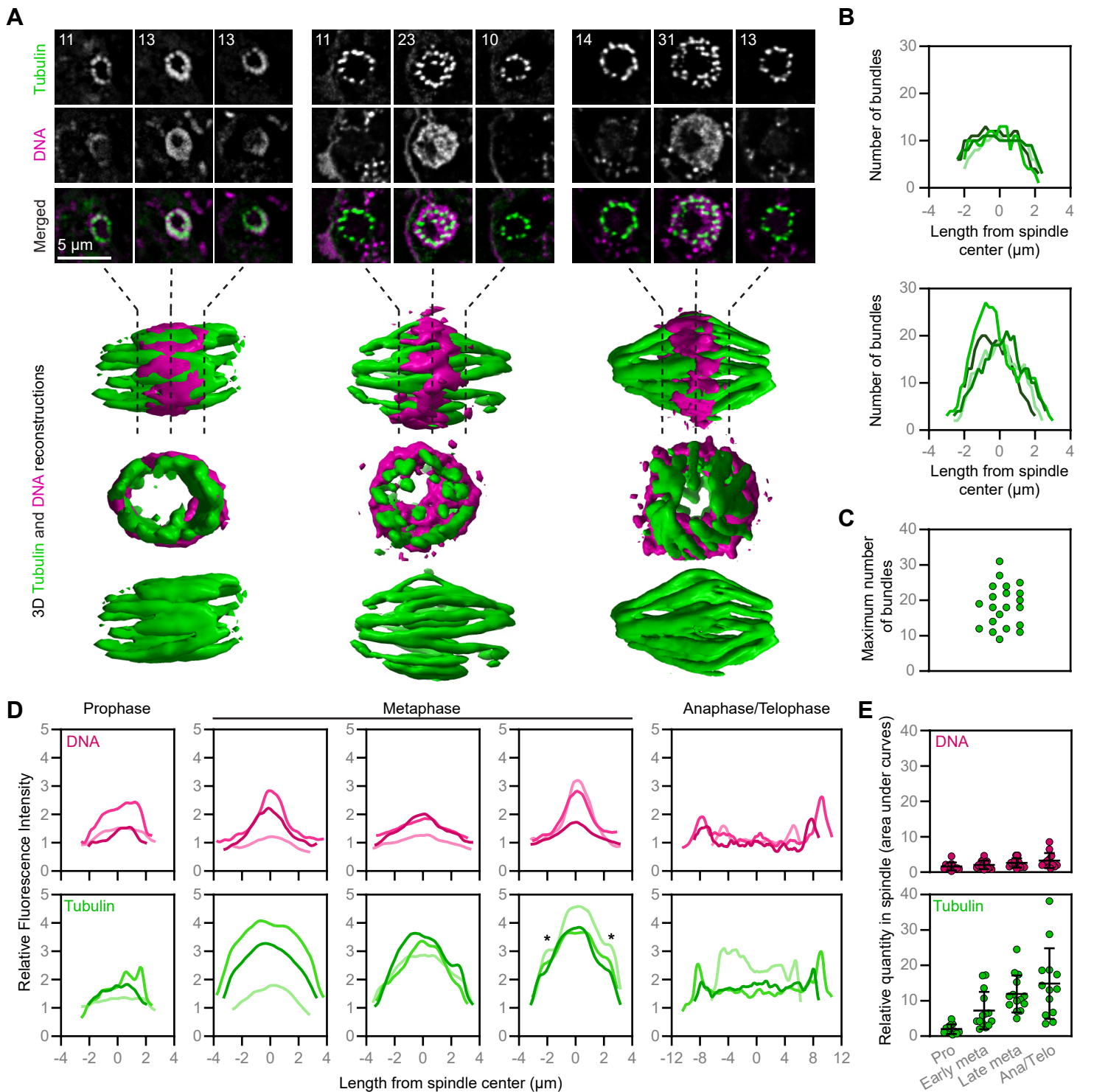


**Figure 4. The number of microtubule bundles changes as mitosis proceeds. (A)** Cells were fixed and stained with antibodies (anti- $\alpha$  tubulin clone DM1A, green) to detect microtubules, and DAPI to label DNA (magenta). Cells with spindles perpendicular to the coverslip were imaged using confocal microscopy and deconvolved using Autoquant software (top panels), and 3D reconstructions were rendered using ChimeraX software (bottom panels, not to scale). Individual Z planes are shown for slices approximately 25, 50, and 75% through the spindle for three representative cells. Numbers (upper left) indicate the number of distinct microtubule bundles in that position of the spindle. **(B)** The number of microtubule bundles throughout the spindle length in metaphase spindles, imaged as in (A). Some spindles (top) had a fairly consistent number of microtubule bundles throughout the spindle ( $n=4$ ), while other spindles (bottom) had a peak in the number of bundles towards the midpoint ( $n=4$ ). **(C)** The maximum number

of microtubule bundles from confocal images of metaphase cells. **(D)** Line scans show the relative DNA and tubulin fluorescence intensity from sum intensity projections of spindles lying in the plane of the coverslip, imaged as in (A). Metaphase spindles were grouped based on the shapes of tubulin curves (no shoulders, left; unclear shoulders, center; two clear shoulders denoted by asterisks, right); three individual examples are shown in each panel (also see Fig. S6). **(E)** Quantification of DNA (top) or tubulin (bottom) from line scans obtained as in (D). Metaphase was categorized as early or late based on the presence (late) or absence (early) of shoulders (stages where no clear classification could be assigned were excluded). Each point represents the area under the curve for one spindle line scan, and lines indicate the mean  $\pm$  SD.

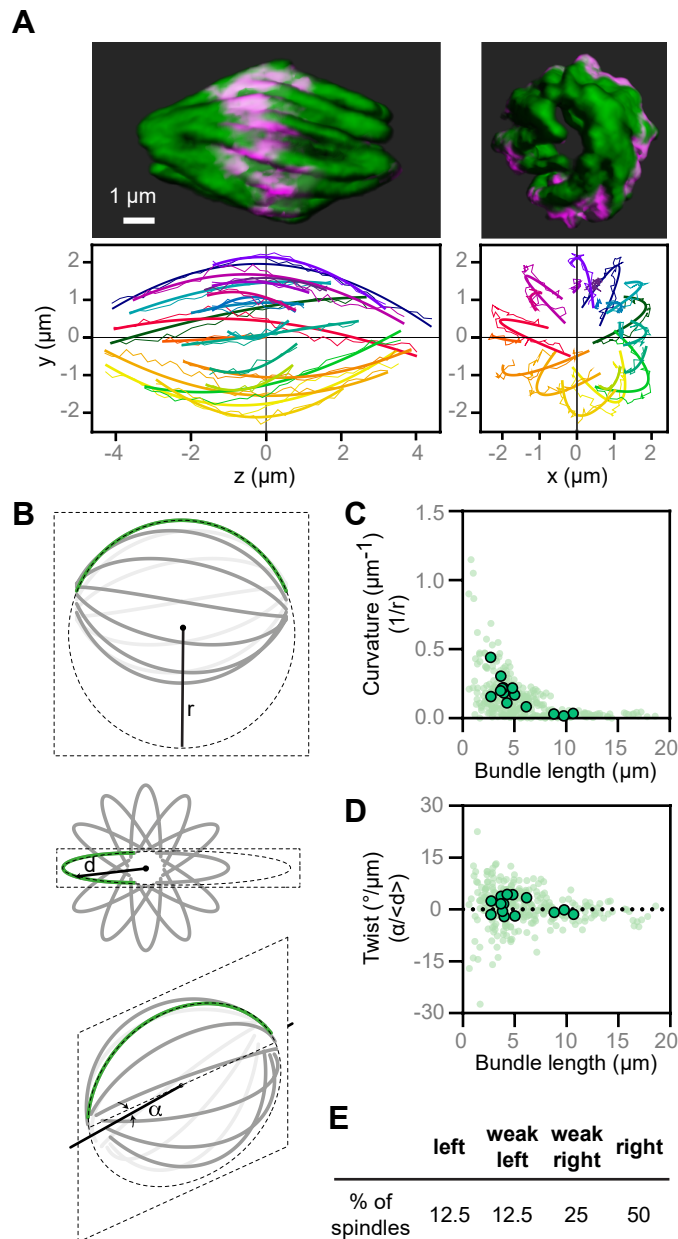


**Figure 5. *Naegleria* mitotic spindles are twisted.** (A) A 3D reconstructed spindle (the same spindle shown in Fig. 4A, right) is shown from side and end-on view viewpoints. Microtubules are shown in green, and DNA is in magenta. Microtubule bundles were quantified from the side view (left graph) and end-on view (right graph). Each bundle is represented by a different color, thin lines mark the manually traced points along the bundle, and thick lines show circular arcs of the fitted circles. (B) A simplified scheme of a spindle is shown from the side (top), end-on (middle), and from an arbitrary angle (bottom). A microtubule bundle (green line) is fitted by a circle (dashed ellipse) of radius ( $r$ ). The angle ( $\alpha$ ) between the central spindle axis (solid line) and the plane in which the fitted circle lies (dashed parallelogram) is denoted. The distance ( $d$ ) of the bundle from the central spindle axis is denoted. (C) The curvature of microtubule bundles is shown as a function of bundle length (measured along its pole to pole axis). Each small dot represents a single bundle within a spindle, while each larger dot represents the average for a spindle. (D) The twist of microtubule bundles is shown as a function of bundle length. Each small dot represents a single bundle within a spindle, while each larger dot represents the average for a spindle. (E) The percentage of spindles with right, weak right, left, or weak left handedness are shown (see Fig S7 for a breakdown of this analysis).

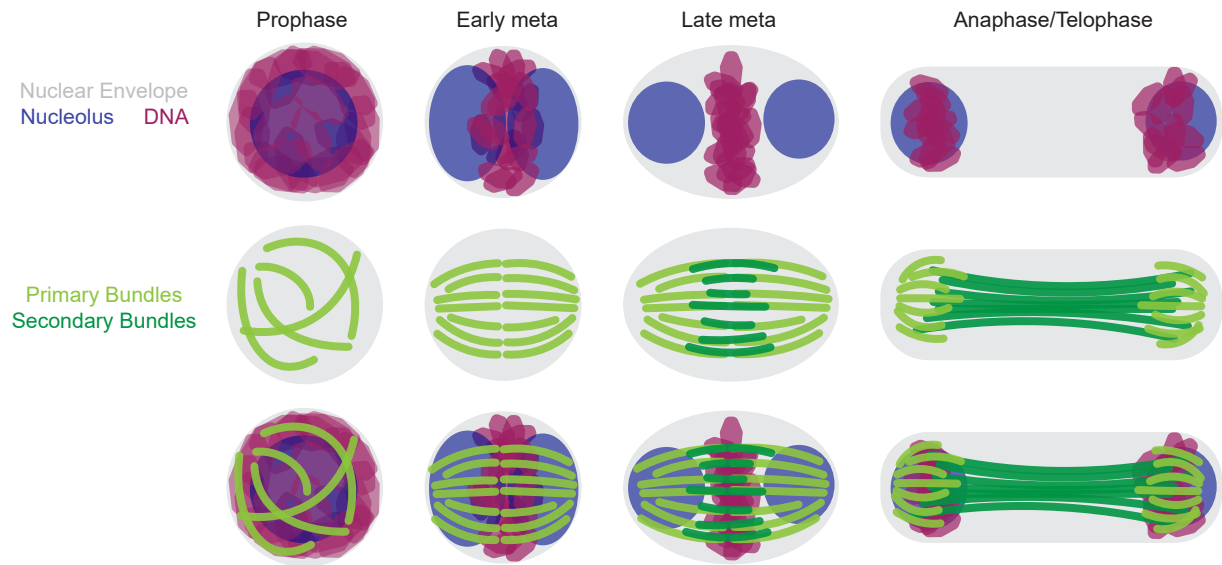


**Figure 6. Model for mitosis in *Naegleria*.** During prophase in *Naegleria*, bundles of microtubules form around a hollow sphere of DNA (magenta) which surrounds the single, round nucleolus (blue). In early metaphase, the DNA condenses into a disk, the nucleolus begins to divide and the microtubule bundles (light green) organize into a hollow, twisted barrel shape. In late metaphase, the DNA is further condensed, and the nucleolus resolves into two distinct spheres. A secondary set of microtubules forms in the equatorial region (dark green) adjacent to the primary bundles. During anaphase/telophase, the DNA is segregated to the two ends of the spindle and the spindle elongates. See text for details.